*nanomaterials*

MDPI

*Article*

# Self-Assembly Synthesis of the $MoS_2$/PtCo Alloy Counter Electrodes for High-Efficiency and Stable Low-Cost Dye-Sensitized Solar Cells

**Zhi Zeng [1], Dongbo Wang [1,*], Jinzhong Wang [1,*], Shujie Jiao [1,*], Yuewu Huang [1], Sixiang Zhao [1], Bingke Zhang [1], Mengyu Ma [1], Shiyong Gao [1], Xingguo Feng [2,*] and Liancheng Zhao [1]**

[1] Department of Optoelectronic Information Science, School of Materials Science and Engineering, Harbin Institute of Technology, Harbin 150001, China; zengzhi_1997@163.com (Z.Z.); huangyuewu703@163.com (Y.H.); auspice123@163.com (S.Z.); zhangbingke007@163.com (B.Z.); wangdong165@sina.com (M.M.); gaoshiyong@hit.edu.cn (S.G.); lczhao@hit.edu.cn (L.Z.)

[2] National Key Laboratory of Science and Technology on Surface Engineering, Lanzhou Institute of Physics, Lanzhou 730000, China

* Correspondence: wangdongbo@hit.edu.cn (D.W.); jinzhong_wang@hit.edu.cn (J.W.); shujiejiao@hit.edu.cn (S.J.); fengxingguo10@163.com (X.F.)

Received: 5 August 2020; Accepted: 27 August 2020; Published: 31 August 2020


**Abstract:** In this work, $MoS_2$ microspheres/PtCo-alloy nanoparticles ($MoS_2$/PtCo-alloy NPs) were composited via a novel and facile process which $MoS_2$ is functionalized by poly (N-vinyl-2-pyrrolidone) (PVP) and self-assembled with PtCo-alloy NPs. This new composite shows excellent electrocatalytic activity and great potential for dye-sensitized solar cells (DSSCs) as a counter electrode (CE) material. Benefiting from heterostructure and synergistic effects, the $MoS_2$/PtCo-alloy NPs exhibit high electrocatalytic activity, low charge-transfer resistance and stability in the cyclic voltammetry (CV) and electrochemical impedance spectroscopy (EIS) test. Meanwhile, a high power-conversion efficiency (PCE) of 8.46% is achieved in DSSCs with $MoS_2$/PtCo-alloy NP CEs, which are comparable to traditional Pt CEs (8.45%). This novel composite provides a new high-performance, stable and cheap choice for CEs in DSSCs.

**Keywords:** $MoS_2$/PtCo-alloy nanoparticles; dye-sensitized solar cells; counter electrodes; efficiency; electrocatalytic activity

## 1. Introduction

DSSCs have been regarded as one of possible alternatives to silicon photovoltaics, owing to their sustainable energy and competent power-conversion efficiency (PCE), low cost, facile fabrication process and environmental friendliness [1,2]. Normally, a sandwich structure of DSSCs consists of a photoanode sensitized by dye sensitizers, counter electrodes and electrolytes containing triiodide/iodide ($I_3^-/I^-$). There have been extensive studies of the essential components of DSSCs, such as photoanodes [3,4], dye sensitizers [5–7], electrolytes [8,9] and counter electrodes (CEs) [10,11]. Among them—as the catalyzers of redox couple and electrodes—CEs are expected to have imperative characters, such as high electrocatalytic activity, good electron-conduction ability and stability [12,13]. Platinum (Pt) with excellent performance on conductivity and electrocatalytic activity has been widely used as CE materials [14]. However, the traditional iodine-based electrolyte can corrode Pt into $PtI_4$ on the surface of electrode [15,16] leading to relatively low PCE and instability of DSSCs. Moreover, the high price and high temperature annealing of Pt CEs limits the industrialization of DSSCs. To alternate

Pt CEs, many kinds of materials have been developed, such as cheap metals [17], alloys [18–26], polymers [27,28], carbon materials [29–32] and transition metal compounds [33–35].

Developing composite counter electrodes which consist of two or more materials are novel and effective way to improve the performance and lower the cost [36]. Generally, composite CEs can be divided into Pt-loaded composite CEs and Pt-free composite CEs. Normally, Pt-loaded composites are made by loading Pt nanoparticles on the low-cost materials. In this way, the electrocatalytic activity of composites are improved. Pt-free composites are the combination of carbon materials, transition metal compounds and polymers. Generally, the electrocatalytic activity of Pt-free composites is higher than single materials due to synergetic effects of diverse materials in composites.

Molybdenum sulfide ($MoS_2$) as a typical transition metal compound possesses many attractive properties, such as a triatomic layer structure, atomic-scale thickness, high catalytic activity and outstanding stability [36,37]. $MoS_2$ is mainly applied in the field of hydrodesulfurization (HDS) [38] and hydrogen evolution reaction (HER) [39] as a high-performance catalyst because there are active sites for catalyst on the edges of triatomic layers [40]. For DSSCs, Wu et al. synthesized leaf-like $MoS_2$ as CEs which exhibited prominent catalytic activity for $I_3^-/I^-$. In this research, the DSSCs with $MoS_2$ CEs showed the PCE of 7.59%, comparable to that of Pt (7.64%) [33]. Recently, in addition, many further studies concentrated on $MoS_2$ composited with inorganic compounds or carbonaceous materials, because the edges of $MoS_2$ layers restrict the number of active sites. Through hybridizing or compositing $MoS_2$ with other materials, such $MoS_2$/C [41], $MoS_2$/graphene [42,43], $MoS_2$/CNTs [44], $MoS_2$/NiS [45], Co–Mo–S [46], Fe–Co-$MoS_2$ [47] could achieve higher catalytic activity and lower charge resistance.

On the other side, thanks to the outstanding electrocatalytic activity and relatively low cost of nano alloys (NAs), many kinds of NAs have been used to substitute for traditional Pt CEs [48]. NAs which are metallic materials synthesized by several metals or metals/metalloids on the nanoscale are pretty different from single metals and bulk metals on characters and catalysis performance. For NAs, many properties are better than single metals and bulk metals on the field of electrocatalysis, such as high surface energy, plentiful active sites and stability. These properties are associated with nanosized effects, abundant defects and reconfigurable electronic structures, respectively [49]. As for the application of NAs in the CEs of DSSCs, numerous kinds of NAs not only displayed excellent catalytic activity, chemical stability and synergistic effects, but also effectively reduced the costs of CEs. NAs include Pt-transition metal alloys: PtRu [50], PtCo [18], PtNi [51,52], PtFe [53,54], PtMo [55,56], PtCr [55], PtPd [55,57], PtZn [58], PtCoFe [59], PtCoNi [19]; Pt-free alloy: CoSe [60], CoNi [61], NiSe [62], CoPd [63], FeNi [64], FeSn [65].

To date, both NAs and $MoS_2$ exhibits high performance as the CEs of DSSCs, however, few studies have investigated the $MoS_2$/PtCo-alloy nanoparticles (NPs) composite CEs. In this article, $MoS_2$ microspheres with the flake-like surface were facilely synthesized by the hydrothermal route. PtCo-alloy NPs were prepared via the co-reduction. Moreover, the uniform and controllable self-assembly between $MoS_2$ and PtCo-alloy NPs based on hydrogen bonding networks was achieved by poly (N-vinyl-2-pyrrolidone) (PVP). The novel composite shows more active sites, excellent electrocatalytic activity and stability through electron microscopy, electrochemical impedance spectroscopy (EIS) and cyclic voltammetry (CV). A notable PCE of 8.46% was achieved and it is comparable to that of the DSSCs with Pt CEs. The synthesis strategy of the $MoS_2$/PtCo-alloy NP composite is effective and also have promising prospects in area such as electromagnetic shielding [66] and solar to steam generation [67–69].

## 2. Materials and Methods

### *2.1. Materials and Reagents*

Thiourea ($CH_4N_2S$), sodium molybdate ($Na_2MoO_4{\cdot}2H_2O$), chloroplatinic acid hexahydrate ($H_2PtCl_6{\cdot}6H_2O$), cobalt(II) chloride ($CoCl_2$), sodium borohydride ($NaBH_4$), ethylene glycol ($C_2H_6O_2$),

titanium(IV) tetrachloride ($TiCl_4$), acetonitrile ($C_2H_3$ N) and lithium perchlorate ($LiClO_4$) were purchased from Shanghai Aladdin Bio-Chem Technology Co., Ltd. (Shanghai, China). Poly (N-vinyl-2-pyrrolidone) (PVP K30) was purchased from Beijing Solarbio Biologic Technology Co., Ltd. (Beijing, China) 4-tert-butyl-pyridine (TBP), 1,3-dimethylimidazolium (DMII), iodine ($I_2$), guanidinium thiocyanate (GNCS) and lithium iodide (LiI) were purchased from Sigma-Aldrich (St. Louis, MO, USA). All agents are analytical grade and used without any purification. The sensitized dye N719 was purchased from Dyesol. FTO glass (2.2 mm, 15 Ω/square, Nippon Sheet Glass, Tokyo, Japan) was divided into rectangles with a size of 2 × 1.5 $cm^2$ and successively washed in detergent, deionized water and ethanol with the ultrasonic bath.

### 2.2. Synthesis of $MoS_2$ Microspheres

The method of synthesizing $MoS_2$ microspheres by using micelle template is described previously [50]. First, the PVP solution was obtained by dissolving 0.4 g of PVP (K30) into 80 mL of deionized water and stirring 30 min. Then, 1.92 g of thiourea and 0.96 g of $Na_2MoO_4{\cdot}2H_2O$ were dissolved into as-prepared PVP solution by stirring 30 min. Next, the reaction solution was transferred into a 100-mL Teflon-lined stainless-steel autoclave and heated for 24 h at 200 °C. After the hydrothermal reaction finished, the black dispersion was collected by centrifugation at 7000 rpm for 15 min, wished two times with deionized water and dried at 60 °C in vacuum.

### 2.3. Synthesis of the $MoS_2$/PtCo-Alloy NP Composite Material

The detailed strategy of fabricating the $MoS_2$/PtCo-alloy NP composite is as follows 0.5 g of as-prepared $MoS_2$ was dispersed into ethylene glycol (EG) by stirring 30 min. Then, 0.1 g of PVP was dissolved into the dispersion. After stirring 30 min, a certain amount of $H_2PtCl_6$ and $CoCl_2$ (molar ratio of $H_2PtCl_6$:$CoCl_2$ = 1:1) was added into the mixture with stirring and ultrasonic bath for 30 min. Then, a full amount of $NaBH_4$ was gradually added into the prepared mixture. After stirring for 5 h, the composite was extracted by centrifuging and washing the mixture. The obtained composite was finally dried at 60 °C for 12 h in vacuum.

### 2.4. Preparedness of Counter Electrodes

The fabrication of $MoS_2$-based CEs and Pt CEs follows different methods. The preparation of $MoS_2$-based CEs was adhered to the precedent research [25]. The as-prepared $MoS_2$-based materials was mixed with carbon black and PVDF at the ratio of 8:1:1 (mass ratio). The mixture was dispersed into NMP. Moreover, the dispersion was grinded until the dispersion turned to slurry with appropriate viscosity. Then, the doctor blade method was used to coat the as-obtained slurry on FTO glass. In this method, prepared solution was dropped on FTO glass, then the doctor blade was used to scrape dropped solution to form smooth and uniform film on the surface of FTO. Finally, the obtained glass with solution film heated at 500 °C for 10 min with a heat gun, in this way, CE was fabricated successfully. The material-coated FTO counter electrodes were dried at 60 °C for 12 h in vacuum and were annealed at 500 °C for 2 h in argon.

Pt CEs as a matched group in our experiments were fabricated as a traditional method. Brief, 10-mM $H_2PtCl_6$ in isopropanol was coated on FTO glass by doctor blade method and heated at 500 °C for 10 min with a heat gun.

### 2.5. Fabrication of DSSCs

The process of photoanodes and DSSCs fabrication was described like previously studies [70,71]. To begin with, a $TiO_2$ blocking layer was formed on FTO glass by soaking washed FTO glass into a 40-mM $TiCl_4$ aqueous solution and heating at 70 °C for 30 min. Afterwards, a $TiO_2$ layer was coated on the pretreated FTO glass by screen printing. The thickness of $TiO_2$ layer was controlled by the times of repeating the screen printing. Subsequently, the $TiO_2$ film was roasted at 450 °C for 30 min and natural cooled in air. When it cooled down to 120 °C, the anode was immersed into 0.5-mM N719 acetonitrile

and tert-butanol (1/1, *v/v*) solution for 24 h. Next, as-prepared anodes and counter electrodes were attached to the sandwich structure by hot-pressing with Surlyn films. Then, the iodine-based electrolyte which is the acetonitrile solution composed of 0.60-mM DMII, 0.03-M I2, 0.10-M GNCS and 0.50-M TBP was injected into the sandwich structure.

### *2.6. Characterization*

The micrographs of materials were taken by the field-emission scanning electron microscope (FESEM, HITACH SU70, Tokyo, JPN) and the high-resolution transmission electron microscope (HRTEM, FEI, Tecnai G2 F30). X-ray diffraction (XRD) analysis was achieved by an X-ray diffractometer (Empyrean, Panalytical, Malvern, UK) with Cu-K$\alpha$ radiation. A X-ray photoelectron spectrometer (ESCALAB250Xi, Thermo Fisher, Waltham, MA, USA) was employed in finishing the X-ray photoelectron spectra (XPS) analysis.

### *2.7. Electrochemical and Photovoltaic Measurements*

All the electrochemistry measurements were implemented on an electrochemistry workstation (CHI660e, Chenhua instruments Ins., Shanghai, China). The cyclic voltammetry (CV) was conducted to estimate the performance of counter electrodes. This measurement system consists of three electrodes (a Pt auxiliary electrode, an Ag/AgCl reference electrode and a 3 $cm^2$ of working electrode) and iodine-based electrolyte which is the acetonitrile solution containing 10-mM LiI, 1-mM $I_2$ and 0.1-M $LiClO_4$. The electrochemistry impedance spectroscopy (EIS) was measured with symmetric dummy cells composed of double identical counter electrodes. Moreover, they were injected the electrolyte which was same as the DSSCs electrolyte in our experiments. The active area of dummy cells was controlled at 0.64 $cm^2$.The frequency range of EIS was from 1 Hz to $10^5$ Hz. Moreover, tests were at 0.01 V of bias voltage and in dark. The photocurrent density–voltage (*J–V*) curves of the DSSCs were measured by the electrochemistry workstation. The simulative solar light (100 $mW{\cdot}cm^{-2}$, AM 1.5) was produced by a Xe lamp (cel-S500/350, Beijing China Education Au-light Co., Ltd., Beijing, China).

## 3. Results

To investigate the crystal structure of samples, a series of XRD tests were conducted. The XRD patterns of $MoS_2$ microspheres and $MoS_2$/PtCo-alloy NP composites are shown in Figure 1.

Among different types of samples, $MoS_2$/PVP means the fresh material which was synthesized by the PVP micelle-assisted hydrothermal route and covered by molecular chains of PVP. Moreover, annealed $MoS_2$ was heated at 500 °C for 2 h in argon to remove PVP which can influence the shape and peak positions of XRD patterns. In particular, featured peaks of $MoS_2$ at 14.02° (002 planes) reflect the condition of $MoS_2$ layer stacking (strong peak indicates order stacking of $MoS_2$ layer) [72]. In Figure 1 the (002) peaks of fresh samples shift towards lower angles and that peak of the annealed sample returns to 14.02° and is diminished. The reason of peak shift is molecular chains of PVP between $MoS_2$ layers increase the average spacing between layers. Moreover, the peak of annealed sample is weakened, because residual carbon produced by burning PVP turned closely the stacking structure of $MoS_2$ to the approximately single-layer structure. Meanwhile, the $MoS_2$/PtCo-alloy NP composites which contain different amount of PtCo-alloy NPs are denoted as $MoS_2$/5 wt% PtCo, $MoS_2$/10 wt% PtCo and $MoS_2$/20 wt% PtCo. The peaks of XRD patterns roughly accord with figures of hexagonal $MoS_2$ peaks (JCPDS card No.37–1492) and the peak shifts occur obviously on (002), (100) and (110) $MoS_2$ planes. Peak position shifts apparently associate with macromolecular chain of PVP adhering, because the peak positions of $MoS_2$ become more accordant for the standard hexagonal $MoS_2$ pattern after samples were removed PVP by annealing. The (111) diffraction peak of PtCo-alloy NPs is also exhibited in Figure 1. A distinct shift of the Pt (111) diffraction peak towards a higher degree owing to the shrinking lattices of PtCo. Pt atoms substituted by smaller Co atoms normally leads to contraction of PtCo lattices which coincides with previous results [73].

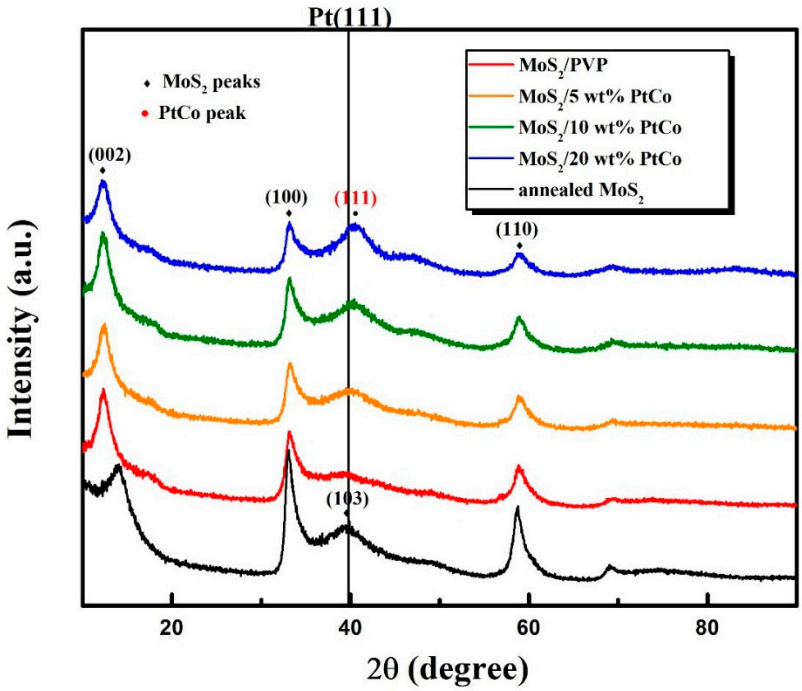


**Figure 1.** XRD patterns of $MoS_2$ microspheres and $MoS_2$/PtCo-alloy nanoparticle (NPs) composites.

FESEM and TEM images of $MoS_2$ microspheres and $MoS_2$/PtCo-alloy NP composites synthesized by different methods are shown in Figures 2 and 3, respectively. $MoS_2$ microspheres which are composed by vertical $MoS_2$ nanoflakes expose edges of nanoflakes on the surface of microspheres. This structure is beneficial to improve the catalytic activity because more edges are exposed on the surface of $MoS_2$ microspheres. In the TEM images of $MoS_2$ microspheres, many molecular chains of PVP covered microspheres. The PVP-functionalized $MoS_2$ microspheres create the precondition for self-assembly of $MoS_2$/PtCo-alloy NP composites.

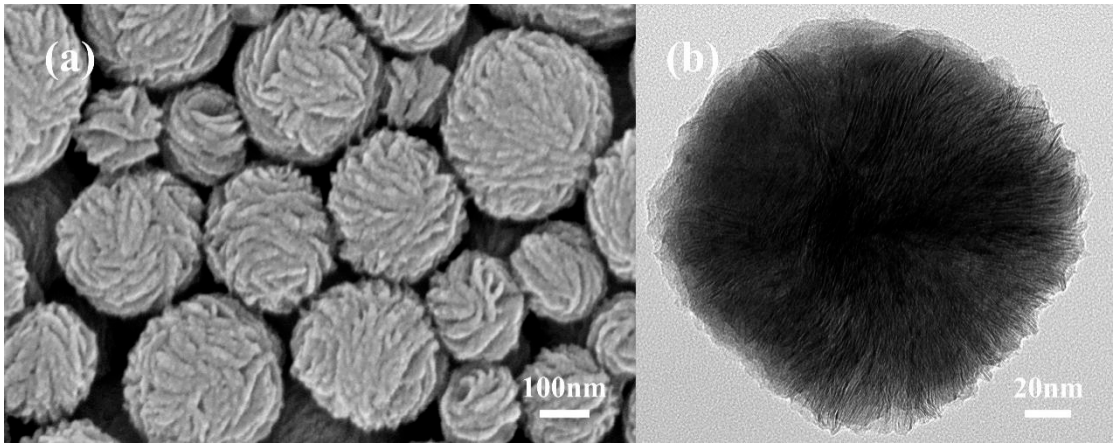


**Figure 2.** Morphologic characterizations of $MoS_2$ microspheres prepared by the poly (N-vinyl-2-pyrrolidone) (PVP) micelle-assisted hydrothermal method. (**a**) FESEM image; (**b**) low-resolution TEM image.

To synthesize the $MoS_2$/PtCo-alloy NP composites, three different routes were conducted in our experiments, including co-reducing PtCo-alloy NPs directly, adding PVP before co-reduction in aqueous and adding PVP before co-reduction in ethylene glycol (Figure 3). Co-reducing PtCo-alloy NPs in the $MoS_2$ and PtCo precursors directly (Figure 3a,b) leads to less alloys loaded and obvious aggregation.

To increase the amount of loaded alloys and reduce nanoparticles aggregation, we added PVP into the mixed dispersion before co-reduction (Figure 3c,d). PVP can keep noble metal nanoparticles from aggregation [74]. Moreover, functionalized PtCo-alloy NPs can trend to self-assemble on the surface of $MoS_2$, because the hydrogen-bond networks which is established by hydrophilic groups of PVP can draw PtCo-alloy NPs on the surface of $MoS_2$ microspheres. Moreover, ethylene glycol as the solution of reduction reaction can improve reducing effectiveness and dispersibility [75]. Thus, more uniform, highly dispersed and vast PtCo-alloy NPs loaded on $MoS_2$ microspheres (Figure 3e,f).

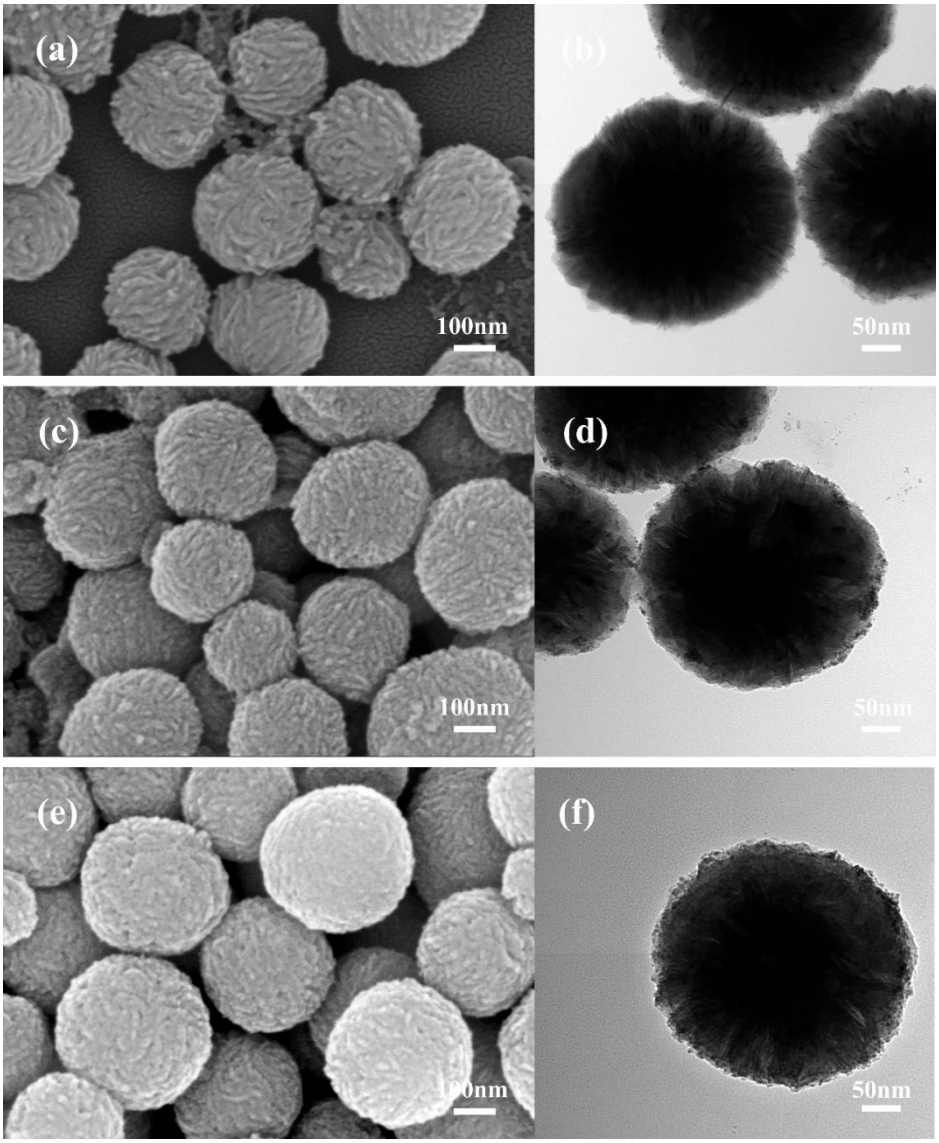


**Figure 3.** FESEM and TEM images of $MoS_2$/PtCo-alloy NP composites (20 wt% PtCo-alloy NPs loading) prepared by different methods. (**a**,**b**) Co-reducing PtCo alloy directly; (**c**,**d**) adding PVP before co-reduction in aqueous; (**e**,**f**) adding PVP before co-reduction in ethylene glycol.

EDX mapping images of $MoS_2$/PtCo-alloy NPs depict that Pt and Co were uniformly dispersed on the surface of $MoS_2$ microspheres as shown in Figure 4b,c, respectively. Additionally, the HRTEM image and XPS further demonstrate the formation of PtCo-alloy NPs. The HRTEM (Figure 4d) indicates the (111) interplanar distance of 0.221 nm was smaller than 0.226 nm which is interplanar spacing of standard Pt (111). This is the other proof that Co atoms enter into the lattices of Pt [76]. Moreover, the Pt 4f peak shifted to higher energies can be obviously observed on the XPS in Figure 5a.

This phenomenon is always associated with alloy formation with Co [77]. There were different work function in Pt and Co. When the combination of them were made to form PtCo alloy, higher atomic ratio of Co to Pt lead to the rehybridization of the d-band and the sp-band, hence, as the reference level in XPS measurements, the change in Fermi level result in the shifting to higher binding energy of Pt 4f peak [78].

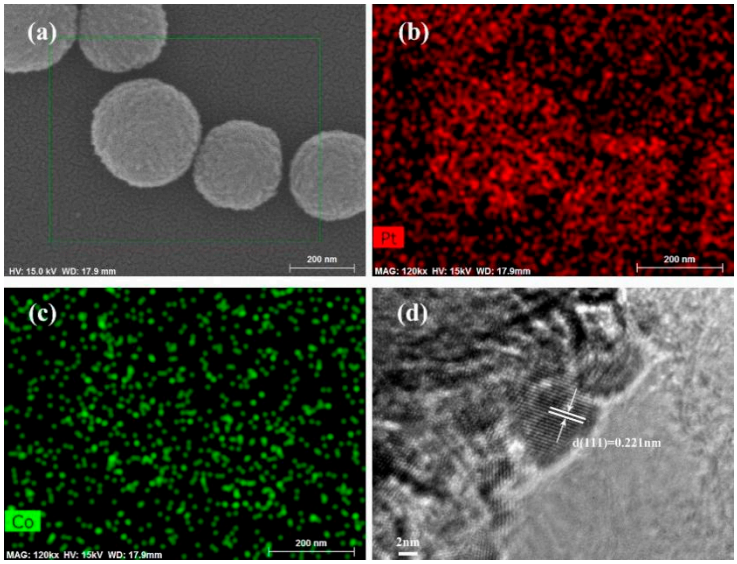


**Figure 4.** EDS mapping images of the $MoS_2$/PtCo-alloy NP composites. (**a**) Mapping area of SEM image; (**b**) element mapping of Pt; (**c**) element mapping of Co; (**d**) HRTEM image of PtCo-alloy NPs.

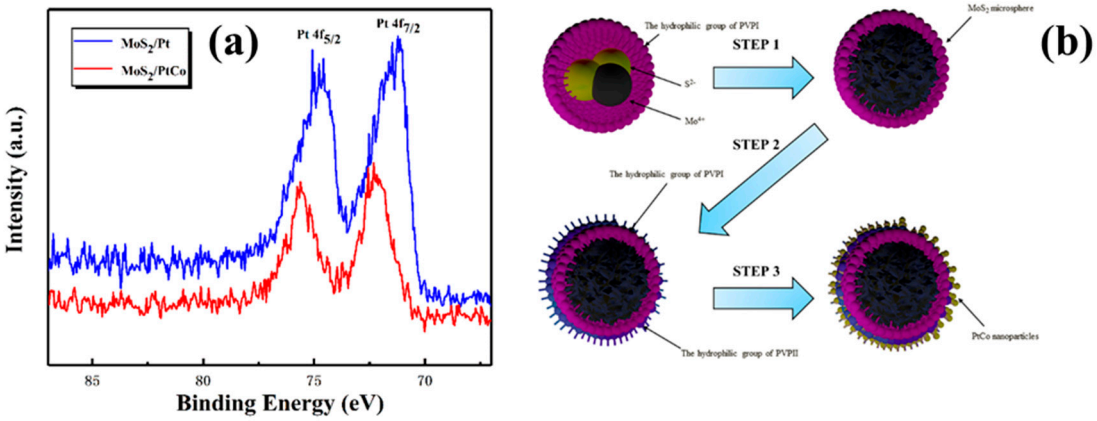


**Figure 5.** (**a**) Pt 4f XPS spectra of $MoS_2$/PtCo-alloy NP composites and $MoS_2$/Pt NPs composites; (**b**) schematic diagram of the process of synthesizing $MoS_2$/PtCo-alloy NP composites.

A typical synthesis route of $MoS_2$/PtCo-alloy NP composites is shown in Figure 5b. Three steps can be concluded for the synthesis of $MoS_2$/PtCo-alloy NP composites. First, micelle-assisted hydrothermal method was carried out to synthesize $MoS_2$ microspheres covered by PVP. This special $MoS_2$/PVP hybrids are easy to disperse and draw more molecular chains of PVP to form the hydrogen bonded networks, because hydrophilic amide groups of PVP on the surface of $MoS_2$ point outward [62]. Thus, when PVP is added for the second time, the new PVP is attracted onto hydrophilic amide groups of primary PVP. Moreover, the new PVP stabilizes PtCo-alloy NPs through coordinating Pt atoms with the N and O atoms of PVP simultaneously [79]. When the co-reduction finishes, PtCo-alloy NPs disperse around $MoS_2$ microspheres. The new PVP acts as "a bridge" to self-assemble PtCo-alloy NPs on the surface of $MoS_2$.

During the process of preparing CEs with doctor blade method, we found that with 5 wt% PtCo and 12 wt% PtCo, surface tension of liquid is large and not easy to spread, so it cannot be wetted and converged on conductive glass. According to repeated experiments, the slurry with 20 wt% PtCo is the easiest to be coated uniformly on the electrode and its performance is also the most ideal. Therefore, CE with 20 wt% PtCo is used for the subsequent electrochemical catalytic activity and photovoltaic performance.

### *3.1. Cyclic Voltammetry Analysis*

Due to the notable improvement of PtCo loading in cells performance, the composites with maximum PtCo loading ($MoS_2$/20 wt% PtCo) in this paper was chosen as the representation of $MoS_2$/PtCo-alloy NP composites to achieve CV and EIS test. At same time, for better lateral comparison, the loading content of pure Pt NPs in $MoS_2$/Pt NPs is also 20 wt%. Cyclic voltammetry (CV) curves (Figure 6a) of $MoS_2$/PtCo-alloy NP composites, $MoS_2$/Pt NPs composites, $MoS_2$ microspheres, and traditional Pt electrodes in $I_3^-/I^-$ electrolyte were measured at a scan rate of 100 mV $s^{-1}$ from −0.8 V to 1.4 V. Two couples of oxidation and reduction peaks are detected. The high potential peak which can be ascribed to the Reaction (1). Moreover, the low potential peak which is mainly related to performance of DSSCs is attributed to the Reaction (2) [80].

$$2I_3^- \boxtimes 3I_2 + 2e^- \quad (1)$$

$$3I^- \boxtimes I_3^- + 2e^- \quad (2)$$

The cathodic peaks potentials of $MoS_2$/PtCo-alloy NP composites, $MoS_2$/Pt NPs composites, $MoS_2$ microspheres and pure Pt electrodes are −0.415 V, −0.495 V, −0.520 V and −0.320 V, respectively. The cathodic peaks potential of $MoS_2$/PtCo-alloy NP CEs is slightly larger than that of Pt CEs, but the redox current density of $MoS_2$/PtCo-alloy NP CEs is slightly larger than Pt CEs. These indicators show $MoS_2$/PtCo-alloy NP CEs possess similar electrocatalytic activity and reaction velocity to Pt CEs.

The charge-transfer mechanism of the $I_3^-/I^-$ system on CE was investigated by scanning CVs at series of scan rates (Figure 6b). For $MoS_2$/PtCo-alloy NP composite CEs, the cathodic peaks (corresponding to $I_3^- + 2e^- \leftrightarrow 3I^-$) and the anodic peaks (corresponding to $3I_2^- + 2e^- \leftrightarrow 2I_3^-$) regularly shifted towards negative direction and positive direction, respectively. The linear relationship between redox peak current and square root of scan rate is shown in Figure 6c. This relationship is acquired by measuring CVs with different scan rates and record the current density of peaks. It indicates only diffusion of $I_3^-/I^-$ ion pair limits redox reactions between the $MoS_2$/PtCo-alloy NPs CE and electrolyte [81].

Taking repeated CV scans of CEs is a routine method to simulate DSSCs in a long time running. The extent of peak shifts in CVs curves strongly associated with electrocatalysis reduction and chemical degradation. The 100 times continuous CVs for $MoS_2$/PtCo-alloy NP composites is shown in Figure 6d. The shape of the CVs curve is highly stable through repeated CVs test, attributing to the excellent electrochemical stability of $MoS_2$/PtCo-alloy NP composites.

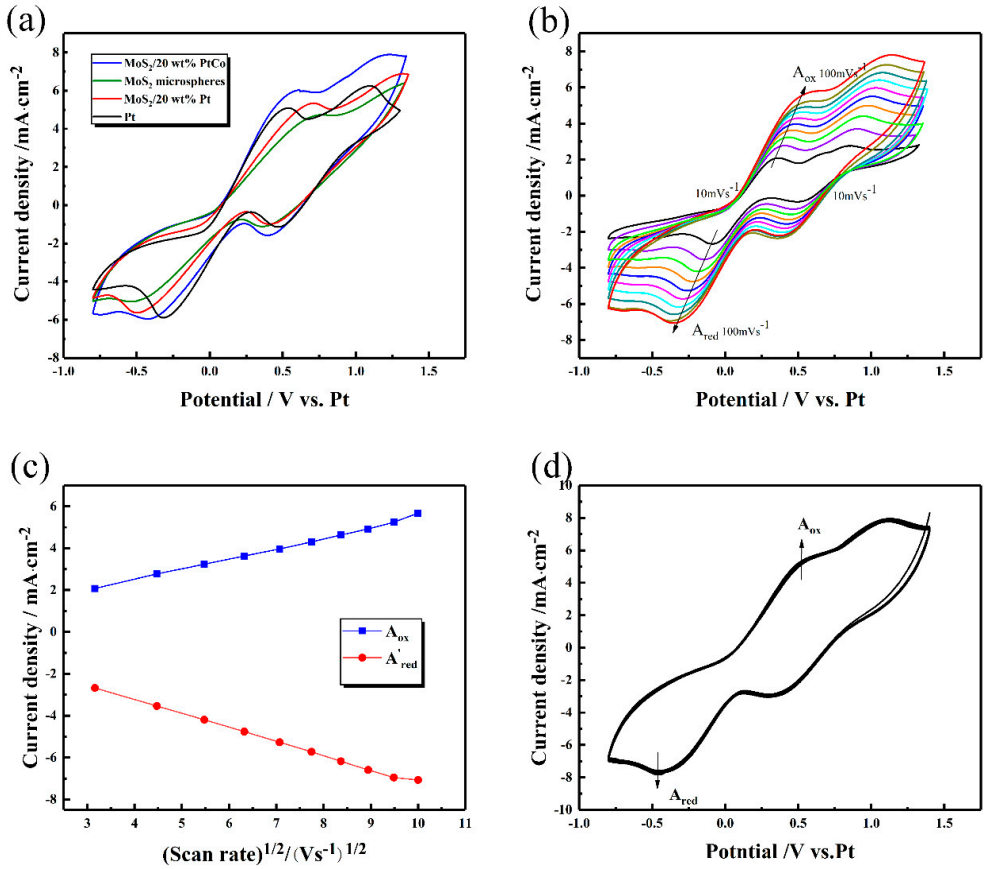


**Figure 6.** (**a**) Cyclic voltammetry (CV) for counter electrodes based on the different materials; (**b**) CVs for the $MoS_2$/PtCo-alloy NP composites with different scan rates (from 10 mV $s^{-1}$ to 100 mV $s^{-1}$, at the intervals of 10 $mVs^{-1}$); (**c**) relationship of redox peak current density and square root of scan rate; (**d**) 100-times continuous cycle scan CVs for the $MoS_2$/PtCo-alloy NP composite CEs at a scan rate of 100 mV $s^{-1}$.

### *3.2. Electrochemical Impedance Analysis*

Electrochemical impedance spectra (EIS) is an important tool to analyze the dynamics of reactions in cells and the surface construct of CEs. The internal resistances of DSSCs are usually divided into series resistance ($R_s$), charge-transfer resistance ($R_{ct}$), diffusion resistance ($Z_w$) and constant phase element (CPE). DSSC with $MoS_2$-based CEs had higher $R_s$ values, which could be ascribed to the different preparation technology. The diffusion of iodine-based electrolytes in the alloy composite is so rapid that, over time, the electrolyte diffuses out of the battery. In order to solve this problem, a circular CE smaller than the package area of the battery was prepared. As result of changing the location and area of CE, the electronic transmission of such electrodes was not just through CE being injecting into the electrode clamp, but passing from CE and FTO in turn, then flowing into the electrode clamp. The FTO was less conductive than CE, therefore, the existence of this process in $MoS_2$-based CEs lead to higher $R_s$ compared with Pt CE. Among them, the $R_{ct}$ of CE/electrolyte is an index to evaluate the electrocatalytic activity, because the small $R_{ct}$ signifies low overpotential and high electron transferring bet ween electrolyte and CEs. Figure 7 shows the Nyquist plots of dummy cells consisted of the CE/electrolyte/CE structure. The $R_{ct}$ values of $MoS_2$/20 wt% PtCo is 1.04 Ω, which is proximity to that of pure Pt (0.71 Ω), indicating that the electrocatalytic activity of $MoS_2$/PtCo is close to that of pure Pt. Moreover, the $R_{ct}$ values of $MoS_2$/20 wt% PtCo is smaller than that of $MoS_2$/20 wt% Pt (1.76 Ω) and $MoS_2$ microspheres (5.18 Ω). It could be put down to the improvement of catalytic ability and electron transfer ability as the result of the metal nanoparticles filling in lamellar interstitial space. Furthermore, synergistic catalysis also plays a role in reduction of $R_{ct}$. The competent charge-transfer

ability of $MoS_2$/20 wt% PtCo CEs displays in the EIS, owing to synergistic effects and $MoS_2$/PtCo-alloy NPs heterostructure.

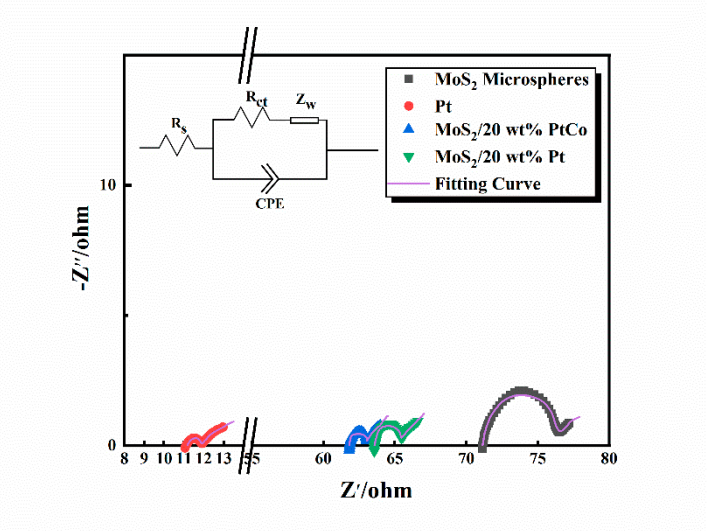


**Figure 7.** Electrochemical impedance spectroscopy (EIS) of dummy cells fabricated with two identical $MoS_2$/20 wt% PtCo, $MoS_2$/20 wt% Pt, $MoS_2$ microspheres, conventional Pt counter electrodes (CEs) and corresponding fitting curves. The equivalent circuit model is inserted in it.

### *3.3. Photovoltaic Performance of DSSCs*

Figure 8 shows the *J*–*V* curves of DSSCs with CEs based different materials. Moreover, all the paraments of photovoltaic performance are exhibited in Table 1. When the $MoS_2$/20 wt% PtCo-alloy NP composite was applicated on the DSSCs as the CE, the DSSCs achieved the impressive conversion of 8.46%, similar to that of Pt CEs. Meanwhile, the DSSCs with the $MoS_2$/PtCo-alloy NP composite CEs possess high short-circuit current ($J_{sc}$), open-circuit voltage ($V_{oc}$) and fill factor (FF) which cannot be gained on the DSSCs with $MoS_2$ CEs. It means there is a significant improvement on the electrocatalytic activity of materials by loading PtCo-alloy NPs on the surface of $MoS_2$. The change in $V_{oc}$ could also be explained by the result of CV. According to formula, the change in redox energy level could influence open-circuit voltage with the relationship of equation:

$$V_{oc} = \frac{KT}{e} ln \frac{J_{inj}}{qek_{et}c_{ox}N_c} + \frac{E_{ref}}{e}$$

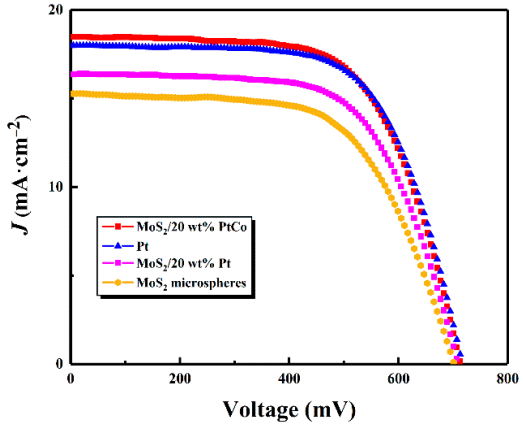


**Figure 8.** *J*–*V* curves of dye-sensitized solar cells (DSSCs) with different counter electrodes.

**Table 1.** Detailed photovoltaic parameters and EIS parameters of DSSCs based on different counter electrodes.

| CE | $J_{sc}$ (mA cm$^{-2}$) | $V_{oc}$ (mV) | FF | PCE (%) | $R_s$ (Ω) | $R_{ct}$ (Ω) |
|---|---|---|---|---|---|---|
| Pure Pt | 17.978 | 718 | 0.655 | 8.45 | 11.17 | 0.71 |
| $MoS_2$/20 wt% PtCo | 18.487 | 715 | 0.640 | 8.46 | 61.69 | 1.04 |
| $MoS_2$/20 wt% Pt | 16.338 | 710 | 0.639 | 7.41 | 63.72 | 1.76 |
| $MoS_2$ microspheres | 15.247 [1] | 703 [2] | 0.616 [3] | 6.61 | 71.32 [4] | 5.18 [5] |

[1] $J_{sc}$—short-circuit current density; [2] $V_{oc}$—open circuit voltage; [3] FF—fill factor; [4] $R_s$—series resistance; [5] $R_{ct}$—charge-transfer resistance.

In which $K$ was molar gas constant, $T$ was temperature, $e$ was elementary charge and $J$ was current density of photogenerated electrons. Symbol $q$ represented the number of electrons during the process of charge transfer with corresponding concentration $c_{ox}$ and transfer rate $k_{et}$. $N_c$ was the density of states of $TiO_2$ conduction band. $E_{ref}$ could be obtained by taking the difference between conduction band edge and the redox potential of the redox coupling electrolyte. Half-wave potentials of $MoS_2$, $MoS_2$/Pt, Pt and $MoS_2$/PtCo CEs measured in CV were 121 mV, 110 mV, 105 mV and 92 mV, respectively, showing the negative shift trend. Therefore, the most negative shift of $MoS_2$/PtCo CEs in the $I_3^-/I^-$ redox energy level resulted in the increase of $V_{oc}$ in DSSCs, leading to the highest $V_{oc}$ [82]. The results of CV showed great consistency in terms of $J$–$V$ curve. The performance gap between $MoS_2$/PtCo CEs and $MoS_2$/Pt CEs is also observed in Figure 8, because the change of electron structure improves the electrocatalytic activity and charge-transfer ability [49].

## 4. Discussion

A new and simple self-assembly method was conducted to synthesize the $MoS_2$/PtCo-alloy NP composite, which was applied to DSSCs as CEs. PVP functionalizes both $MoS_2$ and PtCo-alloy NPs and links each other by hydrogen bonded networks. Finally, the morphology tests investigate that uniform and mass PtCo-alloy NPs were loaded on the surface of $MoS_2$. The structure and composition of $MoS_2$/PtCo-alloy NP composites were studied by XRD, EDS and XPS to prove that PtCo-alloy NPs successfully load on $MoS_2$. Furtherly, the result of CVs and EIS shows the low charge-transfer resistance, outstanding electrocatalytic activity and excellent stability of this material, which is owing to more PtCo-alloy NPs active sites provided and good intrinsic performance of PtCo. Finally, the $J$–$V$ curves were measured under 100 mW cm$^{-2}$ of simulated solar illumination. Moreover, the PCE of 8.46% obtained by the DSSCs with $MoS_2$/PtCo-alloy NP CEs is similar to that of DSSCs based on Pt CEs. Overall, the $MoS_2$/PtCo-alloy NP composite can be regarded as an alternation for the high-cost pure Pt CEs.

**Author Contributions:** Conceptualization, J.W.; methodology, S.Z. and Y.H.; formal analysis, D.W. and Z.Z.; investigation, M.M.; data curation, S.J.; writing—original draft preparation, S.G.; writing—review and editing, B.Z.; supervision, L.Z.; funding acquisition, D.W. and X.F. All authors have read and agreed to the published version of the manuscript.

**Funding:** This research was funded by the National Key Research and Development Program of China, Grant Number SQ2019YFA070104.

**Conflicts of Interest:** The authors declare no conflict of interest.

## References

1. O'Regan, B.; Grätzel, M. A low-cost, high-efficiency solar cell based on dye-sensitized colloidal $TiO_2$ films. *Nature* **1991**, *353*, 737–740. [CrossRef]
2. Grätzel, M. Photoelectrochemical cells. *Nature* **2001**, *414*, 338–344. [CrossRef] [PubMed]
3. Praneetha, S.; Murugan, A.V. Microwave-solvothermal synthesis of various $TiO_2$ nano-morphologies with enhanced efficiency by incorporating Ni nanoparticles in an electrolyte for dye-sensitized solar cells. *Inorg. Chem. Front* **2017**, *4*, 1665–1678.

4. Chen, D.; Huang, F.; Cheng, Y.B.; Caruso, R.A. Mesoporous Anatase $TiO_2$ Beads with High Surface Areas and Controllable Pore Sizes: A Superior Candidate for High-Performance Dye-Sensitized Solar Cells. *Adv. Mater.* **2009**, *21*, 2206–2210. [CrossRef]
5. Balasingam, S.K.; Lee, M.; Kang, M.G.; Jun, Y. A p-Type NiO-Based Dye-Sensitized Solar Cell with an Open-Circuit Voltage of 0.35 V. *Chem. Commun.* **2013**, *49*, 1471–1487. [CrossRef]
6. Shalini, S.; Balasundaraprabhu, R.; Kumar, T.S.; Prabavathy, N.; Senthilarasu, S.; Prasanna, S. Status and outlook of sensitizers/dyes used in dye sensitized solar cells (DSSC): A review. *Int. J. Energy Res.* **2016**, *40*, 1303–1320. [CrossRef]
7. Liu, G.; Kong, L.P.; Yang, W.G.; Mao, H.K. Pressure engineering of photovoltaic perovskites. *Mater. Today* **2019**, *27*, 91–106. [CrossRef]
8. Ye, M.; Wen, X.; Wang, M.; Iocozzia, J.; Zhang, N.; Lin, C.; Lin, Z. Recent advances in dye-sensitized solar cells: From photoanodes, sensitizers and electrolytes to counter electrodes. *Mater. Today* **2015**, *18*, 155–162. [CrossRef]
9. Lee, C.-P.; Ho, K.-C. Poly(ionic liquid)s for dye-sensitized solar cells: A mini-review. *Eur. Polym. J.* **2018**, *108*, 420–428. [CrossRef]
10. Wu, J.; Lan, Z.; Lin, J.; Huang, M.; Huang, Y.; Fan, L.; Luo, G.; Lin, Y.; Xie, Y.; Wei, Y. Counter electrodes in dye-sensitized solar cells. *Chem. Soc. Rev.* **2017**, *46*, 5975–6023. [CrossRef]
11. Tang, Q.; Duan, J.; Duan, Y.; He, B.; Yu, L. Recent advances in alloy counter electrodes for dye-sensitized solar cells. A critical review. *Electrochim. Acta* **2015**, *178*, 886–899. [CrossRef]
12. Wu, M.; Ma, T. Recent progress of counter electrode catalysts in dye-sensitized solar cells. *J. Phys. Chem. C* **2014**, *118*, 16727–16742. [CrossRef]
13. Yuan, H.; Liu, J.; Jiao, Q.; Li, Y.; Liu, X.; Shi, D.; Wu, Q.; Zhao, Y.; Li, H. Sandwich-like octahedral cobalt disulfide/reduced graphene oxide as an efficient Pt-free electrocatalyst for high-performance dye-sensitized solar cells. *Carbon* **2017**, *119*, 225–234. [CrossRef]
14. Longo, C.; De Paoli, M.A. Dye-sensitized solar cells: A successful combination of materials. *Chem. Soc.* **2003**, *14*, 889–901. [CrossRef]
15. Yue, G.; Lin, J.Y.; Tai, S.Y.; Xiao, Y.; Wu, J. A catalytic composite film of MoS2/graphene flake as a counter electrode for Pt-free dye-sensitized solar cells. *Electrochim. Acta* **2012**, *85*, 162–168. [CrossRef]
16. Olsen, E.; Hagen, G.; Lindquist, S.E. Dissolution of platinum in methoxy propionitrile containing LiI/$I_2$. *Sol. Energy Mater. Sol. Cells* **2000**, *63*, 267–273. [CrossRef]
17. Rahman, M.; Kojima, R.; Fihry, M.; Kimura, Y.; Niwano, M. Formation of Porous Titanium Film and Its Application to Counter Electrode for Dye-Sensitized Solar Cell. *Jpn. J. Appl. Phys.* **2010**, *49*, 122302. [CrossRef]
18. He, B.; Meng, X.; Tang, Q. Low-Cost Counter Electrodes from CoPt Alloys for Efficient Dye-Sensitized Solar Cells. *ACS Appl. Mater. Interfaces* **2014**, *6*, 4812–4818. [CrossRef]
19. Yang, Q.; Yang, P.; Duan, J.; Wang, X.; Wang, L.; Wang, Z.; Tang, Q. Ternary platinum alloy counter electrodes for high-efficiency dye-sensitized solar cells. *Electrochim. Acta* **2016**, *190*, 85–91. [CrossRef]
20. Wang, C.; Markovic, N.; Stamenkovic, V. Advanced Platinum Alloy Electrocatalysts for the Oxygen Reduction Reaction. *ACS Catal.* **2012**, *2*, 891–898. [CrossRef]
21. Shao, L.; Qian, X.; Li, H.; Xu, C.; Hou, L. Shape-controllable syntheses of ternary Ni-Co-Se alloy hollow microspheres as highly efficient catalytic materials for dye-sensitized solar cells. *Chem. Eng. J.* **2017**, *315*, 562–572. [CrossRef]
22. Dao, V.D.; Choi, Y.; Yong, K.; Larina, L.L.; Shevaleevskiy, O.; Choi, H.S. A facile synthesis of bimetallic AuPt nanoparticles as a new transparent counter electrode for quantum-dot-sensitized solar cells. *J. Power Sources* **2015**, *274*, 831–838. [CrossRef]
23. Jin, I.-K.; Dao, V.-D.; Larina, L.L.; Choi, H.-S. Optimum engineering of a PtSn alloys/reduced graphene oxide nanohybrid for a highly efficient counter electrode in dye-sensitized solar cells. *J. Ind. Eng. Chem.* **2016**, *36*, 238–244. [CrossRef]
24. Kim, J.-S.; Dao, V.-D.; Larina, L.L.; Choi, H.-S. Optimum alloying of bimetallic PtAu nanoparticles used as an efficient and robust counter electrode material of dye-sensitized solar cells. *J. Alloys Compd.* **2016**, *682*, 706–712. [CrossRef]
25. Dao, V.-D. Bimetallic PtSe nanoparticles incorporating with reduced graphene oxide as efficient and durable electrode materials for liquid-junction photovoltaic devices. *Mater. Today Energy* **2020**, *16*, 100384. [CrossRef]

26. Dao, V.-D.; Larina, L.L.; Tran, Q.C.; Bui, V.T.; Nguyen, V.T.; Pham, T.D.; Mohamed, I.M.; Barakat, N.A.; Huy, B.T.; Choi, H.S. Evaluation of Pt-based alloy/graphene nanohybrid electrocatalysts for triiodide reduction in photovoltaics. *Carbon* **2017**, *116*, 294–302. [CrossRef]
27. Saito, Y.; Kitamura, T.; Wada, Y.; Yanagida, S. Application of poly(3,4-ethylenedioxythiophene) to counter electrode in dye-sensitized solar cells. *Chem. Lett.* **2002**, *31*, 1060–1061. [CrossRef]
28. Wang, H.; Feng, Q.; Gong, F.; Li, Y.; Zhou, G.; Wang, Z. In situ growth of oriented polyaniline nanowires array for efficient cathode of Co (III)/Co (II) mediated dye-sensitized solar cell. *J. Mater. Chem. A* **2013**, *1*, 97–104. [CrossRef]
29. Chang, Q.; Huang, L.; Wang, J.; Ma, Z.; Li, P.; Yan, Y.; Zhu, J.; Xu, S.; Shen, L.; Chen, Q.; et al. Nanoarchitecture of variable sized graphene nanosheets incorporated into three-dimensional graphene network for dye sensitized solar cells. *Carbon* **2015**, *85*, 185–193. [CrossRef]
30. Yue, G.; Wu, J.; Xiao, Y.; Huang, M.; Lin, J.; Lin, Y.J. High performance platinum-free counter electrode of molybdenum sulfide–carbon used in dye-sensitized solar cells. *J. Mater. Chem. A* **2013**, *1*, 1495–1501. [CrossRef]
31. Murakami, T.N.; Ito, S.; Wang, Q.; Nazeeruddin, M.K.; Bessho, T.; Cesar, I.; Liska, P.; Humphry-Baker, R.; Comte, P.; Pechy, P.; et al. Highly efficient dye-sensitized solar cells based on carbon black counter electrodes. *J. Electrochem. Soc.* **2006**, *153*, A2255. [CrossRef]
32. Dao, V.-D.; Choi, Y.; Yong, K.; Larina, L.L.; Choi, H.S. Graphene-based nanohybrid materials as the counter electrode for highly efficient quantum-dot-sensitized solar cells. *Carbon* **2015**, *84*, 383–389. [CrossRef]
33. Wu, M.; Wang, Y.; Lin, X.; Yu, N.; Wang, L.; Wang, L.; Hagfeldt, A.; Ma, T. Economical and effective sulfide catalysts for dye-sensitized solar cells as counter electrodes Transparent metal selenide alloy counter electrodes for high-efficiency bifacial dye-sensitized solar cells. *Phys. Chem. Chem. Phys.* **2011**, *13*, 19298–19301. [CrossRef] [PubMed]
34. Duan, Y.; Tang, Q.; Liu, J.; He, B.; Yu, L. Transparent metal selenide alloy counter electrodes for high-efficiency bifacial dye-sensitized solar cells. *Angew. Chem. Int. Ed.* **2014**, *53*, 14569–14574. [CrossRef]
35. Huo, J.; Wu, J.; Zheng, M.; Tu, Y.; Lan, Z. Effect of ammonia on electrodeposition of cobalt sulfide and nickel sulfide counter electrodes for dye-sensitized solar cells. *Electrochim. Acta* **2015**, *180*, 574–580. [CrossRef]
36. Yun, S.; Hagfeldt, A.; Ma, T. Pt-free counter electrode for dye-sensitized solar cells with high efficiency. *Adv. Mater.* **2014**, *26*, 6210–6237. [CrossRef]
37. Benck, J.D.; Hellstern, T.R.; Kibsgaard, J.; Chakthranont, P.; Jaramillo, T.F. Catalyzing the Hydrogen Evolution Reaction (HER) with Molybdenum Sulfide Nanomaterials. *ACS Catal.* **2014**, *4*, 3957–3971. [CrossRef]
38. Alonso, G.; Berhault, G.; Aguilar, A.; Collins, V.; Ornelas, C.; Fuentes, S.; Chianelli, R.R. Characterization and HDS activity of mesoporous MoS2 catalysts prepared by in situ activation of tetraalkylammonium thiomolybdates. *J. Catal.* **2002**, *208*, 359–369. [CrossRef]
39. Jaramillo, T.F.; Jørgensen, K.P.; Bonde, J.; Nielsen, J.H.; Horch, S.; Chorkendorff, I. Identification of active edge sites for electrochemical $H_2$ evolution from $MoS_2$ nanocatalysts. *Science* **2007**, *317*, 100–102. [CrossRef]
40. Kong, D.; Wang, H.; Cha, J.J.; Pasta, M.; Koski, K.J.; Yao, J.; Cui, Y. Synthesis of $MoS_2$ and $MoSe_2$ Films with Vertically Aligned Layers. *Nano Lett.* **2013**, *13*, 1341–1347. [CrossRef]
41. Zhu, G.; Xu, H.; Wang, H.; Wang, W.; Zhang, Q.; Zhang, L.; Sun, H. Microwave assisted synthesis of MoS2/nitrogen-doped carbon shell–core microspheres for Pt-free dye-sensitized solar cells. *RSC Adv.* **2017**, *7*, 13433–13437. [CrossRef]
42. Fan, M.S.; Lee, C.P.; Li, C.T.; Huang, Y.J.; Vittal, R.; Ho, K.C. Nitrogen-doped graphene/molybdenum disulfide composite as the electrocatalytic film for dye-sensitized solar cells. *Electrochim. Acta* **2016**, *211*, 164–172. [CrossRef]
43. Liu, C.-J.; Tai, S.-Y.; Chou, S.-W.; Yu, Y.-C.; Chang, K.D.; Wang, S.; Chien, F.S.-S.; Lin, J.-Y.; Lin, T.-W. Facile synthesis of MoS2/graphene nanocomposite with high catalytic activity toward triiodide reduction in dye-sensitized solar cells. *J. Mater. Chem.* **2012**, *22*, 21057. [CrossRef]
44. Zheng, M.; Huo, J.; Tu, Y.; Wu, J.; Hu, L.; Dai, S. Flowerlike molybdenum sulfide/multi-walled carbon nanotube hybrid as Pt-free counter electrode used in dye-sensitized solar cells. *Electrochim. Acta* **2015**, *173*, 252–259. [CrossRef]
45. Su, L.; Xiao, Y.; Han, G.; Lin, J.Y. One-step hydrothermal synthesis of feather duster-like NiS@MoS2 with hierarchical array structure for the Pt-free dye-sensitized solar cell. *Nanoparticle Res.* **2018**, *20*, 115. [CrossRef]

46. Zheng, X.; Guo, J.; Shi, Y.; Xiong, F.; Zhang, W.H.; Ma, T.; Li, C. Low-cost and high-performance CoMoS4 and NiMoS4 counter electrodes for dye-sensitized solar cells. *Chem. Commun.* **2013**, *49*, 9645. [CrossRef]
47. Xu, C.; Jiang, Y.; Yang, J.; Wu, W.; Qian, X.; Hou, L. Co-Fe-MoSx hollow nanoboxes as high-performance counter electrode catalysts for Pt-free dye-sensitized solar cells. *Chem. Eng. J.* **2018**, *343*, 86–94. [CrossRef]
48. Sim, E.; Park, E.; Dao, V.D.; Choi, H.S. Synthesis of PtSe catalysts using atmospheric-pressure plasma and their application as counter electrodes for liquid-junction photovoltaic devices. *Catal. Today* **2019**, *337*, 126–131. [CrossRef]
49. Fang, H.; Yang, J.; Wen, M.; Wu, Q. Nanoalloy Materials for Chemical Catalysis. *Adv. Mater.* **2018**, *30*, 1–10. [CrossRef]
50. Dao, V.D.; Jin, I.K.; Choi, H.S. Design of PtRu alloy/reduced graphene oxide nanohybrid counter electrodes for highly efficient dye-sensitized solar cells. *Electrochim. Acta* **2016**, *201*, 1–7. [CrossRef]
51. Xiao, Y.; Han, G. Efficient hydrothermal-processed platinum–nickel bimetallic nano-catalysts for use in dye-sensitized solar cells. *J. Power Sources* **2015**, *294*, 8–15. [CrossRef]
52. Bae, K.H.; Dao, V.D.; Choi, H.S. Utility of Pt in PtNi alloy counter electrodes as a new avenue for cost effective and highly efficient liquid junction photovoltaic devices. *J. Colloid Interface Sci.* **2017**, *495*, 78–83. [CrossRef]
53. Nechiyil, D.; Vinayan, B.P.; Ramaprabhu, S. Tri-iodide reduction activity of ultra-small size PtFe nanoparticles supported nitrogen-doped graphene as counter electrode for dye-sensitized solar cell. *J. Colloid Interface Sci.* **2017**, *488*, 309–316. [CrossRef] [PubMed]
54. Omelianovych, O.; Dao, V.D.; Larina, L.L.; Choi, H.S. Optimization of the PtFe alloy structure for application as an efficient counter electrode for dye-sensitized solar cells. *Electrochim. Acta* **2016**, *211*, 842–850. [CrossRef]
55. Tang, Q.; Zhang, H.; Meng, Y.; He, B.; Yu, L. Dissolution engineering of platinum alloy counter electrodes in dye-sensitized solar cells. *Angew. Chem. Int. Ed.* **2015**, *54*, 11448–11452. [CrossRef] [PubMed]
56. Park, E.; Shin, S.; Bae, K.H.; Dao, V.D.; Choi, H.S. Electrochemical catalytic activity of PtxMo1-x alloy nanoparticles applied to the counter electrode of liquid junction photovoltaic devices. *Solar Energy* **2017**, *153*, 126–133. [CrossRef]
57. Lee, W.Y.; Dao, V.D.; Choi, H.S. Shape-controlled synthesis of PtPd alloys as a low-cost and efficient counter electrode for dye-sensitized solar cells. *RSC Adv.* **2016**, *6*, 38310–38314. [CrossRef]
58. Bae, K.-H.; Park, E.; Dao, V.-D.; Choi, H.-S. PtZn nanoalloy counter electrodes as a new avenue for highly efficient dye-sensitized solar cells. *J. Alloy. Compd.* **2017**, *702*, 449–457. [CrossRef]
59. Chiang, C.C.; Hung, C.Y.; Chou, S.W.; Shyue, J.J.; Cheng, K.Y.; Chang, P.J.; Yang, Y.Y.; Lin, C.Y.; Chang, T.K.; Chi, Y.; et al. PtCoFe Nanowire Cathodes Boost Short—Circuit Currents of Ru (II)—Based Dye—Sensitized Solar Cells to a Power Conversion Efficiency of 12.29%. *Adv. Funct. Mater.* **2018**, *28*, 1–9. [CrossRef]
60. Sun, H.; Zhang, L.; Wang, Z.-S. Single-crystal $CoSe_2$ nanorods as an efficient electrocatalyst for dye-sensitized solar cells. *J. Mater. Chem. A* **2014**, *2*, 16023–16029. [CrossRef]
61. Chen, X.; Tang, Q.; He, B.; Lin, L.; Yu, L. Platinum-Free Binary Co-Ni Alloy Counter Electrodes for Efficient Dye-Sensitized Solar Cells $NiSe_2$ as an efficient electrocatalyst for a Pt-free counter electrode of dye-sensitized solar cells. *Angew. Chem. Int. Ed.* **2014**, *53*, 10799–10803. [CrossRef]
62. Gong, F.; Xu, X.; Li, Z.; Zhou, G.; Wang, Z.-S. $NiSe_2$ as an efficient electrocatalyst for a Pt-free counter electrode of dye-sensitized solar cells. *Chem. Commun.* **2013**, *49*, 1437. [CrossRef] [PubMed]
63. Oh, H.-J.; Dao, V.-D.; Choi, H.-S. Cost-effective CoPd alloy/reduced graphene oxide counter electrodes as a new avenue for high-efficiency liquid junction photovoltaic devices. *J. Alloy. Compd.* **2017**, *705*, 610–617. [CrossRef]
64. Sim, E.; Dao, V.-D.; Choi, H.-S. Pt-free counter electrode based on FeNi alloy/reduced graphene oxide in liquid junction photovoltaic devices. *J. Alloy. Compd.* **2018**, *742*, 334–341. [CrossRef]
65. Oh, H.-J.; Dao, V.-D.; Ryu, K.-H.; Lee, J.-H.; Choi, H.-S. FeSn alloy/graphene as an electrocatalyst for the counter electrode of highly efficient liquid-junction photovoltaic devices. *J. Alloy. Compd.* **2018**, *754*, 139–146. [CrossRef]
66. Oh, H.-J.; Dao, V.-D.; Choi, H.-S. Electromagnetic shielding effectiveness of a thin silver layer deposited onto PET film via atmospheric pressure plasma reduction. *Appl. Surf. Sci.* **2018**, *435*, 7–15. [CrossRef]
67. Dao, V.-D.; Vu, N.H.; Yun, S. Recent advances and challenges for solar-driven water evaporation system toward applications. *Nano Energy* **2020**, *68*, 104324. [CrossRef]
68. Dao, V.-D.; Choi, H.-S. Carbon-Based Sunlight Absorbers in Solar-Driven Steam Generation Devices. *Glob. Chall.* **2018**, *2*, 1700094. [CrossRef]

69. Dao, V.-D.; Nguyen, D.C.; Stręk, W. Enthusiastic discussions on solid physic and material science at SPMS2019. *Sci. Technol. Dev. J.* **2020**, *23*, 490. [CrossRef]
70. Shao, J.; Qu, Q.T.; Wan, Z.M.; Gao, T.; Zuo, Z.C.; Zheng, H.H. $NiSe_2$ as an efficient electrocatalyst for a Pt-free counter electrode of dye-sensitized solar cells. *ACS Appl. Mater. Interfaces* **2015**, *7*, 22927–22934. [CrossRef]
71. Huang, Y.; Wu, H.; Yu, Q.; Wang, J.; Yu, C.; Wang, J.; Gao, S.; Jiao, S.; Zhang, X.; Wang, P. Single-Layer $TiO_2$ Film Composed of Mesoporous Spheres for High-Efficiency and Stable Dye-Sensitized Solar Cells. *ACS Sustain. Chem. Eng.* **2018**, *6*, 3411–3418. [CrossRef]
72. Liang, K.; Chianelli, R.; Chien, F.; Moss, S. Structure of poorly crystalline MoS2—A modeling study. *J. Non-Cryst. Solids* **1986**, *79*, 251–273. [CrossRef]
73. Hu, Z.; Yu, J.C. Pt3Co-loaded CdS and TiO2 for photocatalytic hydrogen evolution from water. *J. Mater. Chem. A* **2013**, *1*, 12221–12228. [CrossRef]
74. Xiong, Y.; Washio, I.; Chen, J.; Cai, H.; Li, Z.-Y.; Xia, Y. Poly(vinyl pyrrolidone): A Dual Functional Reductant and Stabilizer for the Facile Synthesis of Noble Metal Nanoplates in Aqueous Solutions. *Langmuir* **2006**, *22*, 8563–8570. [CrossRef]
75. Kim, P.; Joo, J.B.; Kim, W.; Kim, J.; Song, I.K.; Yi, J. NaBH4-assisted ethylene glycol reduction for preparation of carbon-supported Pt catalyst for methanol electro-oxidation. *J. Power Sources* **2006**, *160*, 987–990. [CrossRef]
76. Chang, L.; Li, Y. One-step encapsulation of Pt-Co bimetallic nanoparticles within MOFs for advanced room temperature nanocatalysis. *Mol. Catal.* **2017**, *433*, 77–83. [CrossRef]
77. Yang, T.; Zhu, H.; Wan, M.; Dong, L.; Zhang, M.; Du, M. Highly efficient and durable PtCo alloy nanoparticles encapsulated in carbon nanofibers for electrochemical hydrogen generation. *Chem. Commun.* **2016**, *52*, 990–993. [CrossRef]
78. Yoon, S.-W.; Dao, V.-D.; Larina, L.L.; Lee, J.-K.; Choi, H.-S. Optimum strategy for designing PtCo alloy/reduced graphene oxide nanohybrid counter electrode for dye-sensitized solar cells. *Carbon* **2016**, *96*, 229–236. [CrossRef]
79. Zhangab, Y.; Xu, J.; Xu, P.; Zhu, Y.; Chen, X.; Yu, W. Decoration of ZnO nanowires with Pt nanoparticles and their improved gas sensing and photocatalytic performance. *Nanotechnol.* **2010**, *21*, 285501–285507. [CrossRef]
80. Bhagwat, S.; Dani, R.; Goswami, P.; Kerawalla, M.A.K. Recent Advances in Optimization of Photoanodes and Counter Electrodes of Dye-Sensitized Solar Cells. *Curr. Sci.* **2017**, *113*, 228–235. [CrossRef]
81. Sun, H.; Luo, Y.; Zhang, Y.; Li, N.; Yu, Z.; Li, K.; Meng, Q. In Situ Preparation of a Flexible Polyaniline/Carbon Composite Counter Electrode and Its Application in Dye-Sensitized Solar Cells. *J. Phys. Chem. C* **2010**, *114*, 11673–11679. [CrossRef]
82. Dao, V.-D.; Kim, S.-H.; Choi, H.-S.; Kim, J.-H.; Park, H.-O.; Lee, J.-K. Efficiency Enhancement of Dye-Sensitized Solar Cell Using Pt Hollow Sphere Counter Electrode. *J. Phys. Chem. C* **2011**, *115*, 25529–25534. [CrossRef]